Relationship between pore size and velocity probability distributions in stochastically generated porous media

M. Siena,[1,*] M. Riva,[1,2] J. D. Hyman,[3] C. L. Winter,[2,3] and A. Guadagnini[1,2]

[1]*Dipartimento di Ingegneria Civile e Ambientale, Politecnico di Milano, Piazza L. Da Vinci 32, 20133 Milano, Italy*
[2]*Department of Hydrology and Water Resources, University of Arizona, Tucson, Arizona, 85721, USA*
[3]*Program in Applied Mathematics, University of Arizona, Tucson, Arizona, 85721, USA*

We perform a set of detailed numerical simulations of single-phase, fully saturated flow in stochastically generated, three-dimensional pore structures with diverse porosities (ϕ) and degrees of connectivity, and analyze the probability density functions (PDFs) of the pore sizes, S, and vertical velocity components, w, which are aligned with the mean flow direction. Both of the PDFs are markedly skewed with pronounced positive tails. This feature of the velocity PDF is dictated by the pore structure and determines the shortest travel times, one of the key transport attributes that underpins the success or the failure of environmental remediation techniques. Using a maximum likelihood approach, we determine that the PDFs of S and w decay according to an exponential and a stretched exponential model, respectively. A strong correlation between the key parameters governing the decay of the upper tails of the two PDFs is found, which provides a quantitative result for this analogy that so far has been stated only qualitatively. The parameter governing the concavity of the tail of the velocity PDF varies linearly with porosity over the entire range of tested values ($0.2 \leqslant \phi \leqslant 0.6$). The parameters controlling the spread of the upper tails of the PDFs of S and w appear to be linked by a power-law relationship.

PACS number(s): 47.56.+r, 47.61.−k, 91.60.Np, 47.11.Bc

I. INTRODUCTION

Detailed knowledge of flow and transport in complex porous systems is of relevance in several industrial and environmental applications, ranging from oil recovery to groundwater protection procedures. Recently, Bijeljic *et al.* [1] numerically investigated the non-Fickian behavior of solute transport on millimeter-scale micro-computed tomography (CT) images of a bead pack, a sandstone, and a carbonate sample. The authors showed that the computed propagators relative to mean displacement along the main flow direction (i.e., concentration versus displacement) (i) compare well with nuclear magnetic resonance (NMR)-measured propagators associated with similar conditions, and (ii) depend on the distribution of velocities which is in turn dependent upon the pore-space structure. Previous studies [2–7] explore the effects of diverse pore structures on the distribution of local velocities. However, a clear understanding and quantification of this relationship is still lacking.

Kutsovsky *et al.* [2] analyzed the axial velocity distribution in two bead pack configurations (with porosity, ϕ, approximately equal to 0.4) using NMR images for Reynolds numbers, Re (based on bead diameters), ranging between 14.9 and 44.8. The authors showed that the axial velocity profile is roughly parabolic in the pores. Moreover, the positive tail of its probability density function, PDF, decays exponentially, consistent with predictions obtained from a simple bundle-of-tubes model. Similar results were shown by Lebon *et al.* [3] in experiments performed with extremely low Re numbers (between 0.36 and 1.8) in unconsolidated packings of spherical beads with $\phi = 0.36$.

Maier *et al.* [4] observed a correspondence between NMR measurements and numerical results obtained by the lattice-Boltzmann method (LBM) in different bead packs with $0.37 \leqslant \phi \leqslant 0.43$ and $0.6 \leqslant$ Re $\leqslant 30$. The authors found a qualitative correspondence between the positive tail of pore sizes and velocity distributions, i.e., the longer are the tails of the pore sizes, the longer are those of the velocities.

Van Genabeek [5] adopted LBM to solve for flow in two-dimensional lattices characterized by high ϕ values, ranging from 0.6 to 0.99. The author showed that a stretched exponential model fits the positive tail of the sample velocity distributions, the distribution parameters being strongly related to ϕ. Araújo *et al.* [6] presented numerical flow simulations in two-dimensional random media generated with solid nonoverlapping disks and characterized by high porosity values, $0.6 \leqslant \phi \leqslant 0.9$. The authors noticed a nearly Gaussian distribution of the product between velocity and ϕ^2. On the other hand, they observed PDFs of local fluxes (computed as the convolution of channel widths and velocity distributions) to be represented satisfactorily by a stretched exponential model. Rouyer *et al.* [7] studied the flow of noncolloidal spheres immersed in a quasi-two-dimensional fluidized suspension and found velocity fluctuation PDFs to vary from Gaussian to exponential as particle concentration increases. In summary, existing works in the literature indicate that velocity PDFs in porous samples tend to be characterized by positive tails which decay according to exponential [2–4] or stretched exponential [5,7] models.

Here, we analyze and quantify the correlation between the pore structure and the distribution of the local velocities, which has so far been stated only qualitatively [4–7], using a direct numerical simulation of flow through explicit three-dimensional pore structures. This study is a step toward the identification of analytical relationships that allow the distribution of pore velocity values to be quantified from routine pore size analyses. In particular, we are interested in characterizing the positive tail of the density of the (normalized) velocity component along the mean flow direction, w, due to its critical influence on

*Corresponding author: martina.siena@polimi.it

the distribution of the shortest residence times of dissolved solute particles in the system. The study is performed in synthetically generated isotropic random porous media to investigate the influence of intricate porous microstructures on pore-scale velocity densities under a broad range of realistic porosity values ($0.2 \leqslant \phi \leqslant 0.6$) and Reynolds numbers (from about 1 to more than 400). First, the pore-space generation process is outlined and the resulting porous microstructures are examined in detail (Sec. II A). Next, the numerical method employed to simulate fluid flow through the generated porous microstructures is briefly summarized in Sec. II B. The key results of the numerical simulations are provided in Sec. III. We conclude with some remarks in Sec. IV.

II. MATERIALS AND METHODS

A. Generation of three-dimensional porous media

Isotropic sample blocks of porous media are generated using the procedure implemented in Hyman *et al.* [8], which has been shown to provide realistic three-dimensional pore structures [9], on cubic lattices with side $L = 1.27 \times 10^{-2}$ m and uniform grid step $\Delta l = 10^{-4}$ m. First, a three-dimensional lattice is populated with random variables sampled from the uniform distribution on the closed interval [0, 1]. Then, this field is convolved with a symmetric Gaussian kernel to produce a spatially correlated topography. The geometry of the pore space is determined by assigning nodes in the correlated topography to the void space or to the solid matrix. A level threshold is applied to the resulting topography so that a node is assigned to the void or the solid matrix space if the generated value at the node is, respectively, lower or higher than the threshold. The resulting pore space offers no preferred direction to flow because the topography is isotropic and statically stationary. Three different values of connected porosity, i.e., $\phi = 0.2, 0.4$, and 0.6, and Gaussian kernel parameter, $\sigma = 0.01, 0.03$, and 0.05, are considered. The latter controls the spatial correlation of the void space, as detailed below.

Figure 1 depicts examples of the void distribution along horizontal cross sections in all nine blocks. The samples generated with wider kernels are associated with pore spaces with fewer and wider pores than those obtained with narrower σ values. The connectivity of the void spaces increases with σ. To further explore this aspect and to quantify the range of validity of our analysis, we investigate the spatial correlation of the void space by calculating the variogram of the indicator function, I (where $I = 1$ in the pore voxels and $I = 0$ otherwise). As an example, Fig. 2 shows plots of the variograms, $\gamma_I(h)$, evaluated for $\phi = 0.4$ and the three σ values, versus h, i.e., the spatial separation distance or lag rescaled by the block size L. Similar depictions are obtained for all blocks investigated.

The variograms $\gamma_I(h)$ tend asymptotically to a sill that does not depend on σ, its theoretical value being equal to $\phi(1 - \phi)$. On the other hand, the degree of correlation of the void spaces is dictated by σ. This dependence can be quantified by fitting standard variogram models to $\gamma_I(h)$ and is illustrated by means of maximum likelihood (ML) fits to each $\gamma_I(h)$ (Fig. 2) of spherical variogram models,

$$\gamma(h) = \begin{cases} s\left(\frac{3h}{2r} - \frac{h^3}{2r^3}\right) & \text{for } 0 < h \leqslant r \\ s & \text{otherwise} \end{cases}, \quad (1)$$
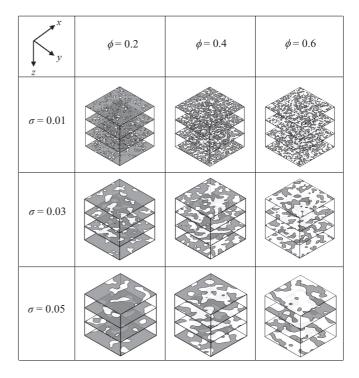

FIG. 1. Example of void distribution along horizontal cross sections in the nine samples. White regions represent the pore space.

where s is the sill of the variogram and r is the (isotropic) range rescaled by the block size L. Similar results were obtained using the exponential model (details not shown). The ML estimates of the parameters s and r are collected in Table I. The range r is almost constant within the porosity range considered and increases almost linearly with σ.

An integral measure of spatial correlation is provided by the integral scale of I, λ (m), defined as

$$\frac{\lambda}{L} = \frac{1}{s} \int_0^\infty [s - \gamma_I(h)] dh. \quad (2)$$

According to Eqs. (1) and (2), $\lambda/L = 3/8\, r$. Table I also reports the ratios L/λ, which indicate that our block samples are associated with sizes ranging from a relatively small
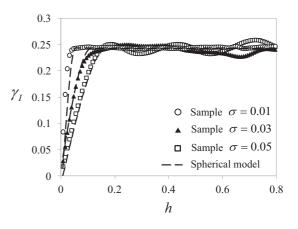

FIG. 2. Sample variograms (symbols) of the indicator function associated with the void space for the blocks with $\phi = 0.4$ for three σ values. Also shown are ML fits with the spherical model [Eq. (1)].

TABLE I. ML estimates of s and r. The length of the side of each cube in terms of integral scales of I, L/λ, is also reported.

σ	ϕ	s	r	L/λ
	0.2	0.15	0.04	71.00
0.01	0.4	0.24	0.04	71.15
	0.6	0.24	0.04	70.85
	0.2	0.16	0.11	25.09
0.03	0.4	0.24	0.11	23.36
	0.6	0.24	0.11	23.52
	0.2	0.16	0.19	14.17
0.05	0.4	0.24	0.16	16.20
	0.6	0.24	0.19	14.35

TABLE II. Topological information of the nine generated blocks.

σ	ϕ	N_{pores}	$\langle C_n \rangle$	$\langle C_n \rangle / N_{\text{pores}}$ (%)
	0.2	3024	3.36	0.11
0.01	0.4	2409	7.31	0.30
	0.6	1453	10.64	0.73
	0.2	215	3.10	1.44
0.03	0.4	171	5.28	3.09
	0.6	107	7.98	7.46
	0.2	49	2.90	5.92
0.05	0.4	49	5.14	10.49
	0.6	39	5.68	14.56

($L/\lambda \approx 15$) to a large ($L/\lambda \approx 70$) number of integral scales of the pore space.

To further characterize the media, we investigate the structure of the pore spaces within a pore-network framework using the maximal ball (MB) algorithm described in [10]. Figure 3 provides renderings of the pore networks obtained for the blocks depicted in Fig. 1. Each pore is associated with a coordination number, which represents the number of pores connected to the pore under consideration. Table II reports the total number of pores (N_{pores}), the average coordination number ($\langle C_n \rangle$) and the ratio $\langle C_n \rangle / N_{\text{pores}}$ for each block. The number of pores decreases with increasing values of σ and ϕ. It appears that σ affects the total number of pores more significantly than ϕ. In particular, N_{pores} decreases by two orders of magnitude as σ increases from 0.01 to 0.05. The average coordination number increases with ϕ, indicating that pores in high-porosity samples exhibit increased local connectivity. The ratio $\langle C_n \rangle / N_{\text{pores}}$ provides a measure of global connectivity in the pore network. This ratio increases
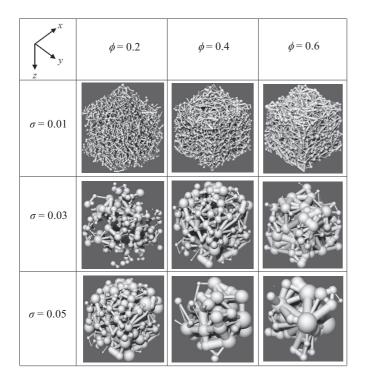
significantly with increasing σ, consistent with the variogram analysis presented above. The values of $\langle C_n \rangle$ obtained in all synthetically generated blocks are similar to those measured on samples of real rocks such as carbonate limestone, and Fontainebleau and Berea sandstone [10–12] with porosity values ranging from 0.1 to 0.6.

B. Pore-scale flow fields

Direct numerical simulations of single-phase, fully saturated flow are performed using a continuous-forcing immersed boundary (IB) approach embedded in the framework of the EULAG software environment [13]. The model adopted in this work is associated with a modified version of EULAG, that has been adjusted and keyed to simulate pore-scale flow in geometrically and topologically complex media [8,14]. EULAG numerically integrates the following set of equations for mass balance and momentum conservation (i.e., Navier-Stokes equations) for an incompressible fluid,

$$\nabla \cdot \mathbf{v} = 0, \tag{3}$$

$$\frac{d\mathbf{v}}{dt} = -\frac{1}{\rho}\nabla p + \mathbf{g} + \upsilon\Delta\mathbf{v} - \alpha\mathbf{v}, \tag{4}$$

where d/dt is the total derivative, $\mathbf{v}$ (m s^{-1}) is the Eulerian fluid velocity vector, p (N m^{-2}) is pressure, $\mathbf{g}$ (m s^{-2}) is the gravitational acceleration vector, and ρ and υ, respectively, are density and kinematic viscosity ($\rho = 10^3$ kg m^{-3} and $\upsilon = 10^{-6}$ m^2 s^{-1} for water). The last term in Eq. (4) represents an additional source whose strength is governed by the parameter α (s^{-1}). This force is activated only at the solid nodes and acts as a repelling force that brings flow velocities to zero within the solid domain. This approach allows for flow simulations to be carried out on uniform Cartesian grids, spanning both the solid and pore-space regions in the domain, and avoids time-consuming meshing procedures.

Equations (3) and (4) are numerically integrated forward in time until steady-state conditions are reached. A key issue to ensure the effectiveness of the approach is the proper selection of the characteristic time scale, α^{-1}, of the IB repelling force. Following [14,15], here we set the time step $\Delta t' = 10^{-5}$ s (and $\alpha^{-1} = \Delta t'/2$), that is, respectively, three and two orders of magnitude smaller than the characteristic time scales associated with the viscous ($=\Delta l^2/\upsilon = 10^{-2}$ s) and gravitational ($=(2\,\Delta l/g)^{1/2} = 4.5 \times 10^{-3}$ s) forces.

FIG. 3. Pore-network descriptions of the blocks reported in Fig. 1.

Flow is forced through the pore space by the pressure gradient imposed by gravity along the vertical direction, z (see Fig. 1 for the coordinate system). We set impermeable boundary conditions on the lateral sides of the samples. These settings reproduce typical flow features occurring in permeameter-like laboratory experimental setups, where the impervious boundary condition along the lateral surface of the laboratory column is ensured by the permeameter cell [1,2,4,7]. Periodic boundary conditions are employed along the top and bottom horizontal sides, thus requiring the medium structure to be periodic along z. Periodicity is achieved by mirroring a generated (nonperiodic) porous medium sample along z, the resulting system being symmetric with respect to the middle horizontal plane. The mirrored porous domain is only used for the purpose of the flow solution (as illustrated, for example, by Hyman *et al.* [9]). All statistical analyses presented in Sec. III are performed on the pore space of the generated pore structures (of size $128 \times 128 \times 128$ voxels). Tests aimed at assessing the influence of the mirroring procedure and of the impermeable conditions set along the block's lateral walls on the key quantities of interest (i.e., pore size and velocity densities) have been performed (details not reported) by analyzing the statistics of interest (according to the methodology described in Sec. III) on inner subdomains obtained by excluding layers of thickness ranging between 8 and 16 voxels from each side of the original blocks. These analyses show that the near wall region associated with the block lateral boundaries and the mirroring procedure do not significantly affect the distribution of the key quantities of interest.

A Lagrangian description of the fluid velocity field is obtained by tracking passive particles through the steady-state velocities evaluated by EULAG. Every node in the void space at the top horizontal cross section is used as an initial position for a particle. Hence, the number of particles for each test case depends on the porosity, as detailed in Sec. III C and in Table V.

A fourth order Runge-Kutta scheme is used to numerically integrate the trajectory equation with a time step $\Delta t = 10^{-5}$ s, until the particle trajectory reaches the bottom of the block or until the total travel time exceeds 10 s. This cutoff time corresponds in each block to at least 20 times the expected breakthrough (or passage) time, $T_{\exp}$ (calculated by dividing the length of the observation domain by the mean vertical flux)

of solute particles. This procedure mimics typical experimental conditions, where the solute breakthrough curve is monitored for a finite time interval corresponding to a multiple of the expected breakthrough time. Some trajectories can be significantly long in both time and space, due to passage through either low-velocity regions of the flow, $O(10^{-16}$ m/s), or a region of recirculation. Some particles might still remain in the system after the observation cutoff time because they are either (i) in low-velocity regions [where local velocities are $O(10^{-16}$ m/s)] or (ii) in a region of recirculation for a very long time.

III. RESULTS AND DISCUSSION

A. Pore size probability distributions

We indicate as *pore size*, S (m), the length of the sequence of consecutive void voxels separating two solid voxels (or separating one solid voxel and a voxel on the block faces) along each of three Cartesian axes, x, y, z (Fig. 1). This is equivalent to the definition of *chord length* provided by Torquato and Lu [16].

The generation method described in Sec. II A produces isotropic pore structures as confirmed by comparing sample pore size probability density functions (PDFs) obtained along different directions (details not shown). Figure 4 shows how the sample PDFs of $S/\Delta l$ (pore size normalized by grid spacing) change with ϕ setting $\sigma = 0.03$ [Fig. 4(a)] and with σ when $\phi = 0.4$ [Fig. 4(b)]. Similar behaviors were obtained for all combinations of σ and ϕ (not reported). All pore size samples are characterized by a pronounced positive skewness of their empirical PDFs. The location (mean) and spread (variance) parameters of these densities increase with ϕ and σ. While the core of the sample distributions is well described by the lognormal model (not shown), their positive tails are best represented by the exponential model

$$f(S/\Delta l) = \alpha_S e^{-\beta_S(S/\Delta l)}. \tag{5}$$

Here, $\alpha_S = \beta_S e^{a_S \beta_S}$ is a normalizing constant, β_S is the model parameter, and a_S is the lower bound of the interval of definition of the exponential distribution, i.e., the threshold value of $S/\Delta l$ above which the pore sizes are interpreted by Eq. (5). The exponential behavior of the positive tail of pore size distributions has also been observed in several samples
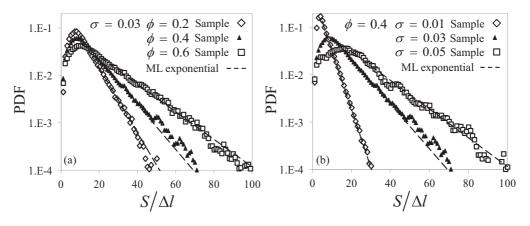

FIG. 4. Probability distributions (PDFs) of $S/\Delta l$ for (a) $\sigma = 0.03$ and (b) $\phi = 0.4$. Symbols represent sample PDFs. Also shown are ML fits of the tails of the distributions with the exponential model [Eq. (5)] (dashed).

TABLE III. ML estimates of the parameters α_S and β_S of the exponential model [Eq. (5)].

σ	ϕ	α_S	β_S
	0.2	1.55	0.48
0.01	0.4	0.56	0.28
	0.6	0.29	0.18
	0.2	0.33	0.16
0.03	0.4	0.18	0.11
	0.6	0.09	0.07
	0.2	0.23	0.11
0.05	0.4	0.11	0.07
	0.6	0.04	0.03

TABLE IV. Mean, variance, coefficient of variation and percentage of negative values of w. The Reynolds numbers of the flow fields are also included.

σ	ϕ	$\langle w \rangle$ (m s^{-1})	σ_w^2 [(m s^{-1})^2]	c_w (%)	$w < 0$ (%)	Re
	0.2	3.79×10^{-3}	5.78×10^{-5}	200	14	1.66
0.01	0.4	2.69×10^{-2}	7.43×10^{-4}	101	7	15.74
	0.6	5.46×10^{-2}	1.69×10^{-3}	75	4	43.04
	0.2	1.14×10^{-2}	7.08×10^{-4}	234	22	12.20
0.03	0.4	5.76×10^{-2}	5.81×10^{-3}	132	19	80.90
	0.6	1.07×10^{-1}	1.00×10^{-2}	94	12	211.80
	0.2	2.08×10^{-2}	1.79×10^{-3}	203	19	33.52
0.05	0.4	9.64×10^{-2}	1.36×10^{-2}	121	19	205.40
	0.6	1.41×10^{-1}	1.97×10^{-2}	100	15	416.95

of real porous media, e.g., [17]. ML fits based on Eq. (5) are depicted in Fig. 4 (dashed lines). ML estimates of β_S (and therefore α_S) are listed in Table III. Goodness of fit of the exponential model [Eq. (5)] is verified on the basis of the Kolmogorov-Smirnov (KS) test [18]. In all cases the sample sizes are particularly large (on the order of 10^5). Therefore, the Hosmer-Lemeshow test for logistic regression models [19] is implemented. The full dataset [of size $O(10^5)$] is divided into groups of equal size (5×10^3) and the KS test is applied to each of these groups. The percentage of subsets for which the KS test is fulfilled (with p values larger than 0.1) ranges between 80% and 100% for all cases.

As reported in Table III, the ML estimates of β_S tend to decrease with ϕ and σ. In other words, the positive tail of the pore size distributions increases with porosity and with the degree of correlation of the pore structure. In particular, Fig. 5 reveals that the coefficient β_S appears to be inversely proportional to the (dimensionless) integral scale of the porosity, λ/L, and to decrease exponentially with ϕ according to

$$\hat{\beta}_S(\phi,\lambda) = C \frac{e^{-k\phi}}{\lambda/L}, \quad C = 0.011, \quad k = 2.5. \quad (6)$$
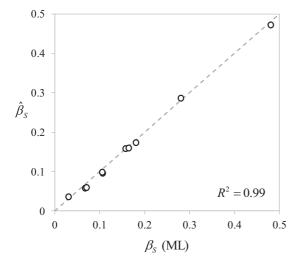

FIG. 5. $\hat{\beta}_S$ estimated by Eq. (6) versus ML estimates of β_S evaluated in the nine samples. The 45° line and the associated determination coefficient R^2 are also reported.

Since the mean value of $S/\Delta l$ is equal to $a_S + 1/\beta_S$ according to Eq. (5), from Eq. (6) one can note that the mean pore size increases linearly with λ/L (and, therefore, linearly with σ) and exponentially with ϕ over the selected generation parameters.

B. Statistical analysis of Eulerian velocity fields

The resulting steady-state velocity fields computed through EULAG are here analyzed to obtain an Eulerian description of the flow statistics. The selected flow configuration (gravity as driving force and impermeable lateral boundaries) results in predominantly vertical flow. The horizontal velocity components are characterized by zero-mean symmetric distributions (details not shown).

Mean, $\langle w \rangle$ (m s^{-1}), variance, σ_w^2 (m^2 s^{-2}), and coefficient of variation, $c_w = \sigma_w/\langle w \rangle$, of the vertical component of velocity, w, are listed in Table IV for all nine blocks. The Reynolds numbers of the flow fields, evaluated as Re $= \langle w \rangle \langle S \rangle / \upsilon$ ($\langle S \rangle$ being the sample average pore size S), are also included in Table IV. We note that $\langle w \rangle$ and σ_w^2 increase with the porosity and with the degree of correlation (i.e., with σ) of the void space. On the other hand, c_w decreases with ϕ, reflecting an increase of the flow uniformity with increasing porosity. The effect of σ on c_w is negligible. Figure 6 depicts the way the sample PDF of the normalized vertical component of velocity, $w/\langle w \rangle$, changes with ϕ for $\sigma = 0.03$ [Fig. 6(a)] and with σ for $\phi = 0.4$ [Fig. 6(b)]. Similar pictures are obtained for all test cases analyzed (not reported). All sample distributions display (i) a pronounced peak around $w = 0.0$, (ii) a marked asymmetry around zero with a pronounced skewness towards positive w values, consistent with the adopted coordinate system (see Fig. 1), and (iii) a decrease of the spread of the distribution with increasing ϕ.

The negative tail of the distributions is formed by values of w that are associated with velocity vectors pointing in the direction opposite to the mean flow (see Fig. 1 for the adopted coordinate system), and are related to the occurrence of reversed flows or recirculation regions within the three-dimensional internal structure of the pore space. The appearance of negative w values has also been observed in laboratory conditions [2] and numerical simulations [4] associated with flow fields through bead packings.

The percentage of void nodes associated with $w < 0$ tends to decrease with increasing porosity and to increase with
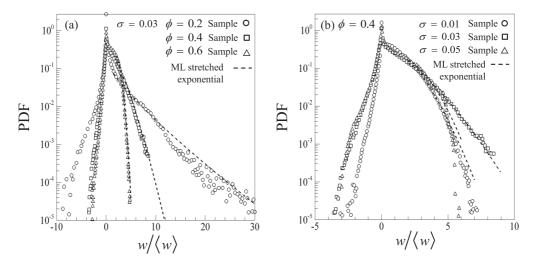
FIG. 6. Probability distributions (PDFs) of $w/\langle w \rangle$, for the blocks generated with (a) $\sigma = 0.03$ and three porosity values and (b) $\phi = 0.4$ and three σ values. Also shown, (dashed) ML fits of the positive tails with the stretched exponential model [Eq. (7)].

σ, as shown in Table IV. Pore spaces characterized by low ϕ and large σ values are related to non-negligible reversed flows or recirculation zones (about 20% of total flow region). The weight of these regions on the overall distribution of w can be linked to the tortuosity (defined in Sec. III C) of the flow trajectories. This aspect is investigated in the following subsection.

C. Lagrangian based statistics

As noted in Sec. II B, the number of the released particles, N_p, is different for the various samples analyzed. Table V reports the value of N_p employed for each block together with N_t, the number of particles that percolate through the observation domain prior to the selected observation time cutoff, which corresponds to about 20 times the expected breakthrough time, $T_{\exp} = L/\langle w \rangle$, as observed in Sec. II B. The trajectory length, l, and the passage time, T, defined as the time taken by a particle to fully percolate through the system, are evaluated for each percolating particle. In all the test cases N_t is sufficiently large to render stable statistics for l and T, with the exception of the test case associated with the smallest porosity and the smallest degree of correlation of void spaces ($\phi = 0.2$ and $\sigma = 0.01$) where almost all particles remain in the sample during the whole observation time ($N_t = 3$).

In all cases the percentage of observed percolating particles increases with ϕ and σ.

Table V lists (i) the mean tortuosity, μ_t (the tortuosity of each trajectory is evaluated as the ratio between l and the side L of the cubic lattice), (ii) the tortuosity variance σ_t^2 and coefficient of variation $c_t = \sigma_t/\mu_t$, (iii) the mean passage time, μ_T, normalized by $T_{\exp}$, (iv) the dimensionless passage time variance, $\sigma_{T/T\,\exp}^2 = \sigma_T^2/T_{\exp}^2$, and coefficient of variation, $c_{T/T\,\exp} = \sigma_T/\mu_T$. The mean tortuosity decreases with ϕ and tends to increase with σ in all cases, although no significant effects can be seen when σ changes from 0.03 to 0.05. The coefficient of variation c_t decreases with ϕ when $\sigma = 0.01$, is almost insensitive to ϕ when $\sigma = 0.03$, and increases with ϕ when $\sigma = 0.05$. Analogous features can be observed for the passage time. Therefore, while the total length of trajectories tends to shorten as the porosities of the media increase, the variability of trajectory lengths strongly depends on the correlation scale of the pore structures. For poorly connected pores, i.e., in the case of $\sigma = 0.01$ (and therefore small Reynolds numbers; see Tables IV and V), the mean tortuosity tends to unity as ϕ increases, indicating straighter trajectories, and tortuosity values tend to cluster around their means as indicated by the small values of c_t. When the pores are well connected, as in the cases associated with $\sigma = 0.05$, as ϕ increases (and Re is particularly high) the variability of

TABLE V. Mean, variance, and coefficient of variation of tortuosities and passage times. The number of released, N_p, and percolating, N_t, particles are also reported.

σ	ϕ	N_p	N_t	μ_t	σ_t^2	c_t (%)	$\mu_T/T_{\exp}$	$\sigma_{T/T_{\exp}}^2$	$c_{T/T_{\exp}}$ (%)
	0.2	2291	3	1.48	1.40×10^{-2}	8	0.68	0.28	78
0.01	0.4	6858	505	1.33	6.00×10^{-3}	6	0.93	0.06	27
	0.6	9757	2388	1.18	3.00×10^{-3}	5	1.04	0.05	21
	0.2	2089	410	1.97	1.10×10^{-1}	17	0.75	0.23	64
0.03	0.4	5986	3355	1.54	7.30×10^{-2}	18	0.96	0.13	37
	0.6	10495	7397	1.37	5.40×10^{-2}	17	1.27	0.14	29
	0.2	2999	1089	2.01	1.15×10^{-1}	17	1.04	0.49	68
0.05	0.4	6476	4838	1.57	1.69×10^{-1}	26	1.08	0.15	36
	0.6	11135	9328	1.58	2.78×10^{-1}	33	1.63	1.15	66

TABLE VI. ML estimates of the parameters α_w, β_w, and γ_w of the stretched exponential model [Eq. (7)].

σ	ϕ	α_w	β_w	γ_w
	0.2	0.29	0.70	0.78
0.01	0.4	0.41	0.44	1.57
	0.6	0.43	0.31	2.44
	0.2	0.15	0.44	0.85
0.03	0.4	0.31	0.39	1.37
	0.6	0.18	0.15	2.68
	0.2	0.20	0.38	1.08
0.05	0.4	0.21	0.23	1.87
	0.6	0.19	0.16	2.48

tortuosity increases and the highest tortuosity values can be observed. This is consistent with the high fraction of negative w values observed in these cases (Sec. III B and Table IV). The increase of the negative tail of w with Re has also been noted by [4] in the range $0.6 < \text{Re} < 30$.

D. Connection between pore structures and velocity fields

In this section we characterize the positive tail of the distribution of the (normalized) vertical velocity component, w, which influences the shortest residence times of dissolved solute particles in the system. In particular, we address the question of whether is it possible to estimate the positive tail of w if only information about the pore structure is available.

Inspection of Fig. 6(a) reveals a marked change of the concavity of the positive tail of the sample PDF of w with the porosity. This feature is captured by the following stretched exponential model [18]:

$$f(w/\langle w \rangle) = \alpha_w (w/\langle w \rangle)^{\gamma_w - 1} \exp[-\beta_w (w/\langle w \rangle)^{\gamma_w}], \quad (7)$$

where $\alpha_w = \beta_w \gamma_w \exp(\beta_w a_w^{\gamma_w})$ is a normalizing constant, β_w and γ_w are the model parameters, and a_w is the lower bound of the interval of definition of the stretched exponential distribution, i.e., the threshold value of $w/\langle w \rangle$ above which the vertical velocities are interpreted by Eq. (7). The choice of the stretched exponential model is supported by the same goodness-of-fit criterion described in Sec. III A. ML fits of Eq. (7) to the tails of sample distributions are depicted by dashed curves in Fig. 6. Table VI lists ML estimates of the set of parameters β_w, γ_w (and therefore α_w) evaluated for all blocks analyzed. The parameter γ_w controls the concavity of the tail and strongly depends on ϕ as shown in Fig. 6(a) and Table VI. The results listed in Table VI indicate that as ϕ increases γ_w ranges from values below unity (indicating a decay of the tail which is slower than exponential) to values larger than 2 (indicating a decay of the tail which is faster than Gaussian).

As mentioned in Sec. I, previous studies observed that (measured and/or simulated) velocities in porous samples tend to be characterized by positive tails which decay according to exponential [2–4] or stretched exponential [5,7] models, consistent with our results. Furthermore, the transition from an exponential to a Gaussian decay (i.e., corresponding to a variation of γ_w between 1 and 2) has been observed qualitatively in [4] for different configurations of sphere packings, in [5] for increasing porosity of synthetic square lattices, and in [7] for decreasing particle concentrations in a suspension (where, considering the analogy between a porous medium and a suspension, a decrease in concentration is interpreted to correspond to an increase in porosity).

Figure 7(a) reports the dependence of ML estimates of γ_w on ϕ obtained for all nine blocks. The estimates of γ_w increase linearly, i.e., $\gamma_w(\phi) = 4.2\phi$ (and therefore the slope of the positive tail of the PDF of w decreases linearly), with ϕ for the broad range (0.2–0.6) of porosities here investigated regardless of σ (i.e., irrespective of the degree of correlation of the pore-space structure). The quality of the linear fit is quantified by the coefficient of determination, R^2, included in the figure, which is close to unity. A similar trend was observed by [5] in high-porosity ($0.6 \leqslant \phi \leqslant 0.99$) two-dimensional lattices.

On the other hand, the parameter β_w of the stretched exponential model contributes together with γ_w to determine the spread of the distribution, which decreases as both γ_w and β_w increase. Figure 7(b) displays the dependence of the ML estimate of β_w on the ML estimate of β_S (obtained from the exponential decay of the pore size distribution) rescaled by the sample porosity, ϕ, on a log-log scale. The data collected in this plot show good agreement with a power-law trend,

$$\beta_w = A \left(\frac{\beta_S}{\phi} \right)^B, \quad A = 0.5, \quad B = 0.42, \quad (8)$$
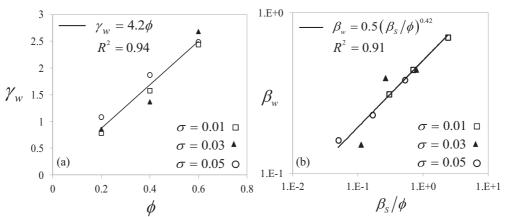

FIG. 7. ML estimates of (a) γ_w versus porosity and (b) β_w versus β_S/ϕ in log-log scale. The regression curves and the associated determination coefficient R^2 are also reported.

as indicated by the high coefficient of determination ($R^2 = 0.91$) reported in the figure. Equation (8) quantifies the rate at which β_w tends to increase (and therefore, for a given ϕ, the way the spread of the velocity distribution decreases) with β_S (which governs the decrease and/or increase of the spread of the pore size distribution) or with the variation of the integral scale of the porosity variogram [as seen by considering jointly Eqs. (6) and (8)]. In particular, for a given ϕ, β_w decreases and the variability of the velocity distribution increases as λ increases, i.e., as the pores are associated with an increased degree of global connection (see also Tables I and II).

IV. CONCLUSIONS AND REMARKS

We generate virtual samples of porous media characterized by different porosity and pore-structure topology. Pore size probability distributions for the generated samples are positively skewed; their positive tails can be properly described by an exponential model [Eq. (5)] and increase as porosity, ϕ, and void space correlation scale, λ, increase. The rate coefficient of the pore distribution decreases linearly with λ and exponentially with ϕ [Eq. (6)]. Numerical simulations of single-phase, fully saturated, gravity driven flow through the generated samples are performed until steady-state conditions are obtained.

The probability distribution of the steady-state vertical velocity component, w, displays a long positive tail and a negative tail. The former can be appropriately modeled by a stretched exponential expression [Eq. (7)], and increases as ϕ decreases, regardless the value of λ. This implies that extremely large (with respect to the mean) values of w (i.e., associated with anomalous short travel times) are more likely to occur in low-porosity rather than in high-porosity systems. The negative tail is related to the occurrence of reversed flows or recirculation regions within the internal three-dimensional structure of the pore space. Systems characterized by small values of ϕ and large λ values are related to a non-negligible fraction of such zones. The importance of these regions on the overall distribution of w can be linked to the tortuosity of the flow trajectories developing in the three-dimensional pore space.

The structure of the PDF of w is complex, depending not only on porosity but also on the pore size probability distribution and, in particular, on its spatial correlation. Nonetheless, the relationship between the parameter γ_w governing the positive tail of the PDF of w and ϕ is linear. We further provide a quantitative relationship describing the way the parameter β_w, which contributes jointly with γ_w to determine the spread of the PDF describing the tail of w, depends on β_s, the key parameter describing the tail of the pore size PDF model.

[1] B. Bijeljic, A. Raeini, P. Mostaghimi, and M. J. Blunt, Phys. Rev. E **87**, 013011 (2013).

[2] Y. E. Kutsovsky, L. E. Scriven, H. T. Davis, and B. E. Hammer, Phys. Fluids **8**, 863 (1996).

[3] L. Lebon, L. Oger, J. Leblond, J. P. Hulin, N. S. Martys, and L. M. Schwartz, Phys. Fluids **8**, 293 (1996).

[4] R. S. Maier, D. M. Kroll, Y. E. Kutsovsky, H. T. Davis, and R. S. Bernard, Phys. Fluids **10**, 60 (1998).

[5] O. van Genabeek, Ph.D. thesis, Massachusetts Institute of Technology, 1998.

[6] A. D. Araújo, W. B. Bastos, J. S. Andrade, Jr., and H. J. Herrmann, Phys. Rev. E **74**, 010401(R) (2006).

[7] F. Rouyer, J. Martin, and D. Salin, Phys. Rev. Lett. **83**, 1058 (1999).

[8] J. D. Hyman, P. K. Smolarkiewicz, and C. L. Winter, Phys. Rev. E **86**, 056701 (2012).

[9] J. D. Hyman, P. K. Smolarkiewicz, and C. L. Winter, Water Resour. Res. **49**, 2080 (2013).

[10] H. Dong and M. J. Blunt, Phys. Rev. E **80**, 036307 (2009).

[11] B. Bijeljic, P. Mostaghimi, and M. J. Blunt, Water Resour. Res. **49**, 2714 (2013).

[12] O. Gharbi and M. J. Blunt, Water Resour. Res. **48**, W12513 (2012).

[13] J. M. Prusa, P. K. Smolarkiewicz, and A. A. Wyszogrodzki, Comput. Fluids **37**, 1193 (2008).

[14] P. K. Smolarkiewicz and C. L. Winter, J. Comput. Phys. **229**, 3121 (2010).

[15] P. K. Smolarkiewicz, R. Sharman, J. Weil, S. G. Perry, D. Heist, and G. Bowker, J. Comput. Phys. **227**, 633 (2007).

[16] S. Torquato and B. Lu, Phys. Rev. E **47**, 2950 (1993).

[17] M. Siena, Ph.D. thesis, University of Trieste, 2013.

[18] A. Clauset, C. R. Shalizi, and M. E. J. Newman, SIAM Rev. **51**, 661 (2009).

[19] P. Paul, M. L. Pennell, and S. Lemeshow, Stat. Med. **32**, 67 (2013).